Comparing signal intensity and refraction sensitivity of double and single mask edge illumination lab-based x-ray phase contrast imaging set-ups

Comparing signal intensity and refraction sensitivity of double and single mask edge illumination lab-based x-ray phase contrast imaging set-ups

G. K. Kallon, P. C. Diemoz, F. A. Vittoria, D. Basta, M. Endrizzi, and A. Olivo

Department of Medical Physics and Biomedical Engineering, Malet Place, London,WC1E 6BT

gibril.kallon.10@ucl.ac.uk

Abstract

Double mask edge illumination (DM-EI) set-ups can detect differential phase and attenuation information from a sample. However, analytical separation of the two signals often requires acquiring two frames with inverted differential phase contrast signals. Typically, between these two acquisitions, the first mask is moved to create a different illumination condition. This can lead to potential errors which adversely affect the data collected. In this paper, we implement a single mask EI laboratory set-up that allows for a single shot retrieval of the differential phase and attenuation images, without the need for a high resolution detector or high magnification. As well as simplifying mask alignment, the advantages of the proposed set-up can be exploited in one of two ways: either the total acquisition time can be halved with respect to the DM-EI set-up or, for the same acquisition time, twice the statistics can be collected. In this latter configuration, the signal-to-noise ratio and contrast in the mixed intensity images, and the angular sensitivity of the two set-ups were compared. We also show that the angular sensitivity of the single mask set-up can be well approximated from its illumination curve, which has been modelled as a convolution between the source spatial distribution at the detector plane, the pre-sample mask and the detector point spread function (PSF). A polychromatic wave optics simulation was developed on these bases and benchmarked against experimental data. It can also be used to predict the angular sensitivity and contrast of any set-up as a function of detector PSF.

1. Introduction

X-ray phase contrast imaging (XPCI) techniques can detect both the phase and attenuation signals from an object. Phase contrast signals arise thanks to x-ray refraction, which tends to occur most strongly at object boundaries. Hence, even weakly attenuating objects, which are invisible to conventional x-ray imaging set-ups, can potentially be detected by XPCI set-ups. The additional contrast provided by XPCI set-ups has been used to target numerous applications, ranging from security, biomedical imaging and material science (Arfelli et al. 1998; Momose 2005; Bravin et al. 2013; Olivo & Robinson 2014; Wilkins et al. 2014). However, these investigations often rely on delicate and sophisticated set-ups that can only be correctly implemented at dedicated research facilities, such as at synchrotrons. Many of these set-ups also use increasingly complex image acquisition procedures to separate differential phase, absorption and ultra-small angle scattering (USAXS) / dark field signals. Such procedures can involve retrieving two or three of these signals from as many exposures acquired under different illumination conditions. For applications with time or dose constraints, this may prove to be impractical since the set-up is subjected to less-than-ideal conditions, such as vibrations and the use of polychromatic x-ray sources with flux limitations. Hence, any prospective XPCI method aiming to target such applications must adequately address the problems mentioned above.

In the last decade, a considerable amount of effort and research interest has been dedicated to developing, and simplifying a number of viable XPCI methods at synchrotrons and in laboratories (Bravin et al. 2013; Olivo & Castelli 2014; Munro 2017). Among the various XPCI implementations, this paper focuses on recent developments to the lab-based edge illumination (EI) XPCI method (Olivo & Speller 2006; Olivo et al. 2011; Ignatyev et al. 2011).

EI is a non-interferometric technique that was first demonstrated with synchrotron sources in the late 90s (Olivo et al. 2001). It was later adapted to commercially available x-ray sources that possess larger focal spot sizes without the need for source collimation. A standard, double mask EI (DM-EI) set-up consists of

two periodic absorbing structures, often referred to as masks, which are placed before the sample and detector respectively. The sample mask, M_1, shapes the incoming x-ray beam into a series of individual beamlets that are separated by the mask period, p_1, whilst the absorbing edges of the detector mask, M_2, are aligned to partially intercept these beamlets. A schematic of the DM-EI set-up is shown in Figure 1. The pre-sample and detector masks are designed to ensure that their magnified periods match the detector pixel pitch.

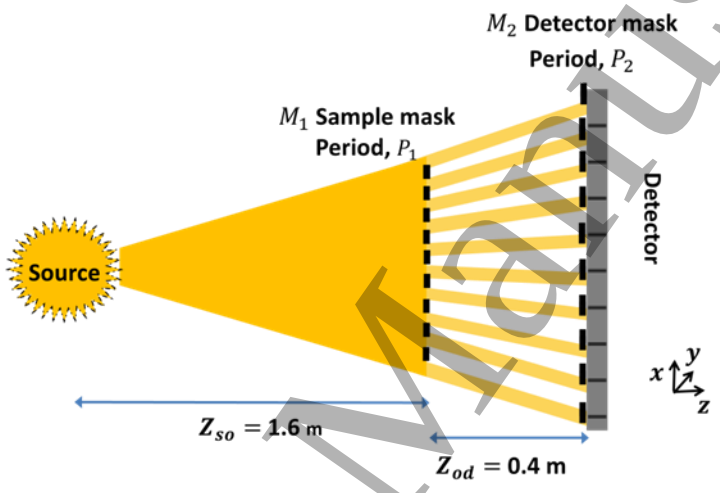

Figure 1 A schematic of a standard, double-mask edge illumination (DM-EI) set-up.

In general, EI set-ups can be characterised by an illumination curve (IC), which is obtained by scanning the pre-sample mask over the span of one period with respect to the detector mask. An intensity variation is recorded for each pixel as a function of sample mask displacement. For the DM-EI set-up, the IC, L_{EI}, measured at the detector mask can be modelled by considering the source and mask parameters of the system:

$$L_{EI}(x) = src\left(\frac{x}{m-1}\right) * M_1\left(\frac{x}{m}\right) * M_2(x); \quad \textbf{(1)}$$

$$m = \frac{z_{so}+z_{od}}{z_{so}}, \quad \textbf{(2)}$$

where $src\left(\frac{x}{m-1}\right)$ represents the source spatial intensity distribution, x represents the co-ordinates at the detector plane and m is the magnification; M_1 and M_2 are the transmission functions of the sample and detector mask, respectively, and $*$ denotes a convolution, which takes place between the source, and the two masks (Endrizzi et al. 2014).

In the presence of a sample, the beams created by M_1 can be attenuated and refracted. To first approximation, attenuation reduces the intensity of the beams falling upon the detector pixels and refraction causes them to be shifted such that the proportion of the beams falling on the detector mask septa is either increased or decreased. These two effects can be individually retrieved by evaluating the changes suffered by the IC, since attenuation can be modelled as a reduction in the area beneath the IC curve, and refraction as a rigid, lateral shift of its centre. Ultimately, both signals lead to changes in the intensity recorded by the pixel with respect to the reference case, i.e. the system without the sample. In fact, since the measured intensity contains mixed contributions from both the refraction and attenuation channels, they can be analytically separated by acquiring two images with the pre-sample mask placed at two different positions: one on either side of the IC maximum. This creates images with inverted differential phase contrast signals but identical attenuation components, which enables phase and absorption separation (Munro et al. 2012).

DM-EI possesses several advantages, e.g. achromaticity (Endrizzi et al. 2015a), relative insensitivity to misalignments (Millard et al. 2013; Endrizzi et al. 2015b), and an ability to work with fairly large, incoherent x-ray sources (Diemoz & Olivo 2014). It has also been repeatedly demonstrated that EI set-ups are largely immune to the effects of vibrations on the order of a few microns. However, the need to acquire two images for differential phase and absorption retrieval can increase the likelihood of errors occurring while positioning the sample or the masks in between the two acquisitions. Furthermore, for some applications, e.g. small animal imaging, shorter acquisition times would be more desirable to reduce the possibility of sample motion, since large positional errors diminish the image quality. While these

additional sources of error can be mitigated by careful data collection and analysis procedures, the ability to perform phase and absorption retrieval by using two frames acquired in a single shot would both speed up and simplify the acquisition procedure. Moreover, it provides opportunities to develop and explore more dose efficient acquisition methods.

For this reason, numerous adaptations have recently been made to the EI system that better exploit its advantages (Endrizzi et al. 2015b; Basta et al. 2015; Vittoria et al. 2015a). Thus far, two such developments have explored the possibility of acquiring sufficient phase-based information with a single exposure. The first approach allows for the retrieval of the projected electron density or thickness of an homogenous sample from a single mixed intensity projection (Diemoz et al. 2015). This single image phase retrieval method uses the free-space propagation and transmission signals in the direction orthogonal to EI sensitivity to enforce consistency between the image columns, thereby eliminating some artefacts that are commonly encountered in 1D phase integration. However, this method assumes a constant δ/β ratio within the sample, where δ is the unit difference of the real part of the refractive index of the sample and β is the imaginary part. For inhomogeneous materials, where the ratio between δ and β is not constant, the approximation breaks down, and ad-hoc tuning of the δ/β parameter is required to achieve the best image quality for selected features only. Another approach, termed “beam-tracking" (Vittoria et al. 2015a; Vittoria et al. 2015b), employs a number of sufficiently small pixels to resolve the individual beamlets and track the changes they experience as a result of their interaction with the sample. By comparing it to the reference case i.e. the beam without the sample, attenuation, refraction and USAXS can be retrieved. However, this method requires a high resolution detector or a high magnification set-up to be effective. These conditions may not always be practical or even achievable. Similar developments have also been made to other existing XPCI methods, which make use of a combination of fine gratings/high resolution cameras, and apply different forms of analysis to retrieve phase contrast information (Wen et al. 2010; Bennett et al. 2010; Morgan et al. 2011; Morgan et al. 2013; Rizzi et al. 2013; Kagias et al. 2016; Zdora et al. 2017).

In the first part of this paper, we implement a simplified approach to single-shot EI XPCI, which addresses some of the limitations of the methods mentioned above, i.e. it does not require any assumption on δ/β, or a high resolution detector. The proposed set-up is a laboratory translation of the edge-illumination set-up, which was first developed by Olivo et al at the synchrotron (Olivo et al. 2001; Olivo et al. 2002), and was later implemented by Krejci et al (Krejci et al. 2010). Data acquired with the proposed set-up is then compared against those acquired with the DM-EI system shown in Figure 1. A number of wire samples (in air) are examined with both EI configurations; the contrast, signal-to-noise ratio (SNR) and refraction sensitivity are also evaluated. This study aims to model and characterise the single mask EI (SM-EI) set-up, to compare it against the DM-EI set-up, and finally, to simulate the signals measured experimentally with both set-ups. In order to achieve this last goal, modifications were introduced to an existing wave optics simulation to enable modelling the various experimental set-ups and conditions. Lastly, the models are validated and are then used to study how the signal and refraction sensitivities of the two EI set-ups vary as a function of detector performance.

2. Methods

The SM-EI set-up uses a sample mask, which defines a set of beamlets that are incident on the detector. Figure 2(a) shows a schematic depiction of the SM-EI set-up; note that the set-up is similar to the one shown in Figure 1 but lacks the detector mask. Instead, the beamlets are aligned so as to fall at the boundary between two pixels. Hence, the edges of individual detector pixels are used to directly "sense" the refraction induced beam displacements (Olivo et al. 2002). For example, Figure 2(b) shows how downward refraction redirects the beam onto pixel 2, thereby increasing its detected counts while simultaneously reducing the beam intensity incident on pixel 1. The opposite would occur for refraction pushing the beam upwards. This alternating illumination condition allows the simultaneous acquisition of two "reversed" refraction images in a single shot (Figure 2(c)), which, as we have previously mentioned, can then be used to perform differential phase and absorption separation.

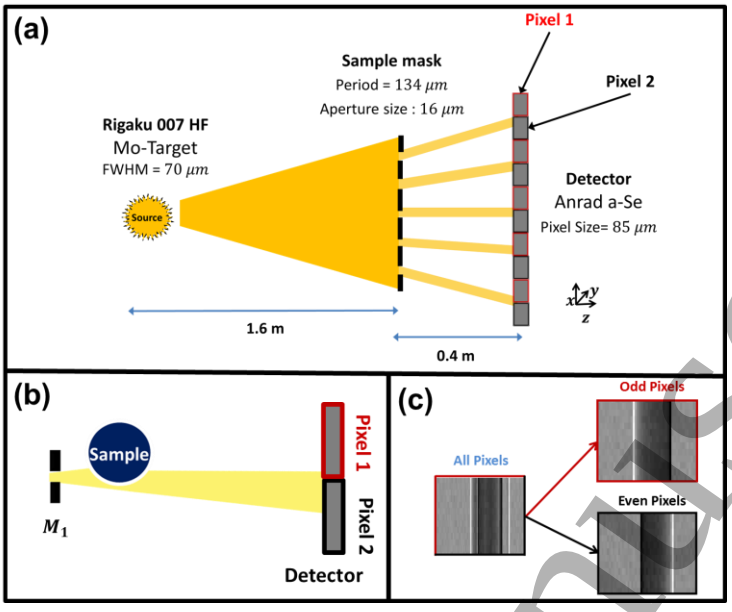

Figure 2 (a) a top-down view schematic of the single-mask EI set-up; the mask apertures define beamlets which are aligned with the edge between two pixels. (b) shows a section of the set-up in (a); however, the addition of a refracting sample causes a displacement of the beamlet. Ultimately, this demonstrates how inverted refraction signals can be simultaneously acquired by separately considering odd and even pixels (i.e. pixels 1 and 2 respectively). (c) shows the mixed intensity image obtained when combining every pixel, as well as the images obtained by separating the odd and even pixels, respectively.

The extraction of the USAXS signal, in a single shot, is not possible with this set-up, as it is with the beam-tracking set-up—where three or more pixels are simultaneously illuminated. In fact, the presence of weak USAXS does not negatively affect the retrieval of the differential phase signal; hence the extraction of USAXS was ignored in this article. The assumption of weak USAXS remains valid as long as the USAXS signal does not cause the beamlets to become wider than a pixel, i.e. the validity of phase retrieval condition breaks down when the beamlets start to overlap. However, the SM-EI set-up uses line-skipped masks (shown by Figure 2(a)) and has so far only been applied direct conversion detectors, which typically have pixel sizes $\geq 50\ \mu m$. These large periods and detector pixel dimension make the limiting

condition difficult to encounter. It is important to note that, in general, line-skipped masks are not required for the DM-EI set-up, but they were used here for the sake of comparing the two set-ups under equivalent conditions.

2.1 Building the experimental set-ups

The set-ups consisted of the Rigaku 007 HF tube source with a rotating molybdenum anode operated at 35 kVp / 25 mA with a focal spot full width half maximum ($FWHM$) = 70 μm, and the Anrad SMAM A-Se detector with 85 μm pixels. The sample and detector masks had periods of $p_1 = 134\,\mu m$ and $p_2 = 167\,\mu m$, and aperture sizes of $a_1 = 16\,\mu m$ and $a_2 = 20\,\mu m$, respectively.

The sample mask was placed at a distance of 1.6 m from the source, and aligned with the detector pixel columns according to the alignment procedure described by Millard et al 2013 (Millard et al. 2013). A misalignment of the mask with respect to the pixel columns would cause non-uniform illumination across the detector. However, this type of misalignment can be corrected by applying local phase retrieval algorithms, which treat sub-sections of the detector independently (Endrizzi et al. 2015b).

Flat field images (images without the sample) can be used to eliminate mask defects and non-uniformities in the detector response/radiation field in the sample image. However, a problem also arises if there is a large drift in the system alignment between the acquisition of a flat field and sample images. In such cases, regions in the sample image that are not occupied by the sample could also be used to devise a partial correction. However, the alignment of the systems used in this study remained constant (within ~2μm over a 5 × 5 cm^2 field of view), between the acquisition of the flat and sample images, thanks to the high tolerance of the set-up (Millard et al. 2013).

The same sample mask was used for both set-ups but the detector mask was added or removed, as required, to switch between the DM and SM-EI set-ups. Masks had a nominal septa thickness of ~30 μm of gold electroplated on 500 μm of graphite. However, it has been shown that the septa thickness can be less than the nominal value if difficulties are encountered during the electroplating process. This leads to

increased unwanted transmission through the mask, which can reduce the sensitivity of the systems by introducing a higher offset to the ICs. Hence, the mask septa thickness had to be independently verified in this study by using the simulation. The SM-EI set-up is particularly sensitive to this effect, since only one mask is used, and therefore, x-rays traverse only one gold layer.

In both SM-EI and DM-EI set-ups, a dithering procedure can be implemented, which increases the spatial resolution of the acquired images by scanning the sample with a number of sub-pixel steps. Indeed, for applications that require a high spatial resolution, the single-mask set-up would require twice as many dithering steps (and therefore twice the exposure time) as a non-skipped DM-EI system in order to match its resolution. However, many biomedical applications do not require a high spatial resolution (Olivo et al. 2013), in which case, the single mask set-up would maintain its higher dose efficiency, as well as its other previously mentioned advantages. For this study, the same skipped sample mask was used to ensure that both set-ups have an equivalent initial spatial resolution. Finally, to ensure that the refraction peaks were sufficiently sampled by both set-ups, 32 dithering steps were used with an exposure time of 30s per step. It is also important to note that the dithering procedure only improves the spatial resolution of an image, but not the statistics acquired within each pixel.

2.2 Adapting the wave optics simulation model for a polychromatic EI set-up

The two experimental set-ups were modelled by modifying an existing wave optics simulation package (Vittoria et al. 2013), with the primary aim of simulating the experimentally measured mixed intensity profiles. This required introducing several new components and features to the wave optics model. A schematic of these modifications is presented in Figure 3. The final model incorporates the source spectrum, and the energy response and point-spread-function (PSF) of the detector. In addition, the absorption from the graphite substrates in the masks, and the cover of the detector were also included (Millard et al. 2014).

The source spectrum data, provided by the manufacturers, were sampled in 0.5 keV steps and the detector energy response was estimated to be linear, to first approximation. This combination of source spectral data and linear assumption for the detector energy response was also used in a previous Monte Carlo model of the EI set-up, which was shown to produce accurate results (Millard et al. 2014). Polychromatic images were obtained by performing multiple monochromatic simulations at given energy steps and taking the weighted average over the spectrum (Olivo & Speller 2006).

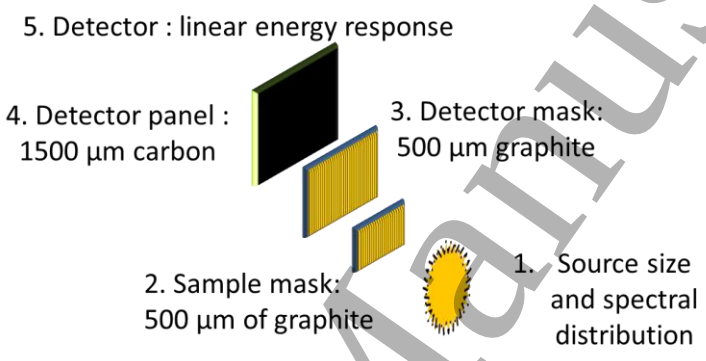

Figure 3 A schematic list of the components that were integrated into the wave optics simulation in order to model both EI and SM-EI set-ups.

2.3 Validating the analytical models of the illumination curve

The first step in validating the simulation involved modelling the SM-EI IC and benchmarking it against the one measured by the real SM-EI system. Since this set-up lacks a detector mask, it requires the addition of the detector PSF into the simulation. An analytical model of the SM-EI IC, L_{SM}, can be expressed as follows:

$$L_{SM}(x) = src\left(\frac{x}{m-1}\right) * M_1\left(\frac{x}{m}\right) * PSF(x), \quad \textbf{(3)}$$

with:

$$PSF(x) = rect\left(x - \frac{w}{2}\right) * \exp\left(-\frac{x^2}{2\sigma_{CS}^2}\right), \quad \textbf{(4)}$$

where $src\left(\frac{x}{m-1}\right)$ represents the projected source size, $M_1(x)$ represents the first mask, and $PSF(x)$ is the measured/simulated detector PSF. The latter has been modelled by smoothing an ideal pixel response (top-hat function) via a convolution with a Gaussian function parameterised by σ_{CS}, its standard deviation. Note that the Gaussian function only represents the effect of charge sharing (CS) in a given pixel and does not necessarily depend on the pixel size. In Eqn. (4), $rect\left(x - \frac{w}{2}\right)$ represents a rectangular function of width w, where w is equal to the pixel size, and centred in 0; thus, it is defined as 1 in the range $(-\frac{w}{2}, \frac{w}{2})$ and 0 elsewhere.

It is worth noting that the PSF does not appear in the expression for the DM-EI IC in Eqn. (1) because the edges of the detector mask apertures redefine the pixel response by introducing a sharp cut-off before the physical edge of the detector pixel. Hence, for DM-EI, the detector mask creates an ideal edge response, while the PSF is generally considered to be a smooth edge. Therefore, for the SM-EI set-up, the sensitivity with which the transition of the beam can be detected, as it shifts between two pixels, depends on the slopes of the detector PSF, and therefore on pixel cross-talk. This charge sharing effect leads to a broader SM-EI IC compared to the DM-EI IC, which is important since the refraction sensitivity in EI is a function of its IC slopes (Diemoz et al. 2013). Consequently, the sensitivity of the SM-EI set-up directly depends on the detector PSF. Greater amounts of pixel cross-talk can be modelled by broadening the Gaussian with which the ideal pixel response is convolved, which leads to a smoother PSF, a gentler IC slope, and ultimately a less sensitive SM-EI set-up.

Since the IC can be used to characterise EI set-ups, it is important for Eqns. (1) and (3) to accurately model the experimentally measured IC. Therefore, the simulation was first benchmarked against a previous, experimentally measured IC acquired at 40 kVp with a DM-EI set-up, which employed an older and well-characterised set of masks. The septa thickness of the masks used in this measurement are

known to be ~28 μm; however, they were also independently determined here by matching the offset of the experimental and simulated IC curves. The result of this comparison is displayed in Figure 4, which also shows a good agreement between the simulation and the real system.

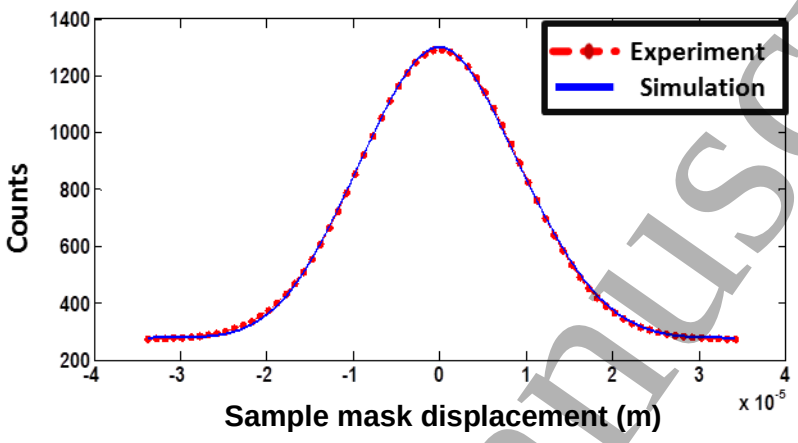

Figure 4 Benchmarking the simulated IC against an experimental IC acquired with a well-known set of masks at 40 kVp.

2.4 Modelling DM-EI and SM-EI signals

To fully characterise the SM-EI set-up, the detector PSF was measured using a standard edge response method (Konstantinidis 2011). The experimentally measured PSF was then fitted with the analytic expression shown in Eqn. (4), which resulted in the extraction of $\sigma_{CS} = 10\ \mu m$ (Figure 5). Note that, as is made clear by Eqn. (4), σ_{CS} does not refer to the width of the measured/simulated PSF, but only to the width of the Gaussian curve used to smooth its first order "ideal" approximation (a box function with $w = 85\ \mu m$).

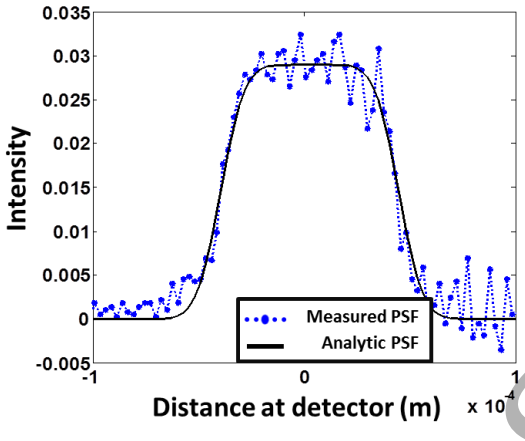

Figure 5 The experimentally measured PSF of the Anrad detector and the analytically fitted function.

The PSF obtained by convolving an ideal box function (i.e. the ideal pixel response function) with a Gaussian function with $\sigma_{CS} = 10\,\mu m$ was then incorporated into the simulations to verify the predictions made by Eqns. (1) and (3), i.e. it can significantly affect the shape of the SM-EI IC but not the DM-EI IC. To demonstrate this, the ICs of both set-ups were simulated using two different PSFs: the experimentally measured value, which was obtained for the Anrad detector, $\sigma_{CS} = 10\,\mu m,$ and an ideal pixel response, i.e. $\sigma_{CS} = 0$. The results are displayed in Figure 6.

Figure 6(a) shows the simulated DM-EI IC, which is obtained by plotting the intensity variation recorded by one set of skipped pixels (odd pixels), while Figure 6(b) shows the SM-EI IC, where one of its "arms" corresponds to signal obtained from one set of skipped pixels (e.g. odd pixels, like pixel 1 in Figure 2 (b)), while the other corresponds to the adjacent ones (e.g. even pixels, like pixel 2 in Figure 2 (b)).

It is apparent from Figure 6(a) that the DM-EI IC remains unchanged, while the SM-EI IC in Figure 6(b) has steeper slopes for an ideal PSF compared to the experimentally measured Anrad case; therefore, the simulated profile of a sapphire wire for the DM-EI set-up remains unaffected by changes in the PSF. Figure 6(c) also demonstrates that the use of a detector with an ideal PSF is equivalent to using a detector mask. Conversely, Figure 6(d) shows that the contrast recorded by the SM-EI set-up for the sapphire wire

decreases for an increased σ_{CS}, which is consistent with the reduced IC slope steepness that is visible in Figure 6(b).

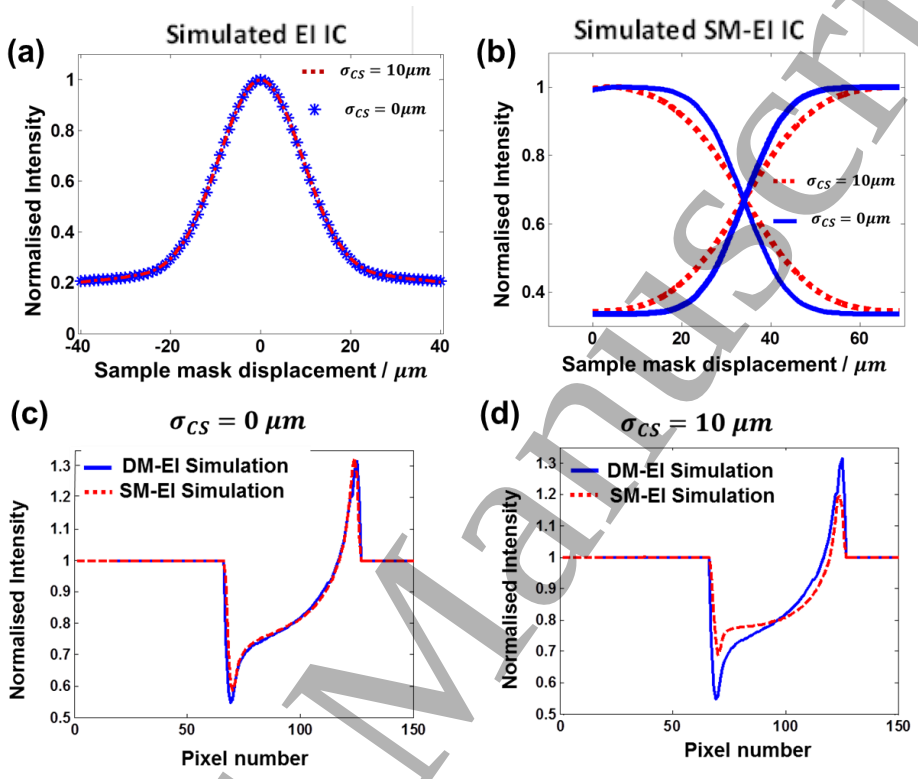

Figure 6 The simulated IC for (a) the DM-EI set-up and (b) the SM-EI set-up using two different PSFs. Simulation of a sapphire wire profile obtained with (c) an ideal detector and (d) a detector with $\sigma_{CS} = 10\ \mu m$, for both set-ups.

These results highlight one advantage of using the detector mask in DM-EI: it mitigates possible negative effects of non-ideal detectors and allows for greater flexibility in constructing the set-up. This also means that for a value of σ_{CS} sufficiently smaller than the pixel size, the mixed-intensity signal recorded with the DM-EI set-up is independent of the detector PSF, while this is not true for the SM-EI set-up.

2.5 Determining the thickness of the mask septa

At this point, the thicknesses of the new mask septa were the only parameters left to be determined, which was done through the model. A two-step process was used, based on comparing the simulated ICs against experimental data. In the first step, the offset of the experimental and simulated ICs for the SM-EI set-up were matched, which allowed the thickness of the sample mask septa to be determined to be $17\mu m$ (Figure 7(a)). This value of the sample mask septa thickness, determined by matching the IC offsets in the SM case, was then used in the second step, where the same procedure was repeated with the DM-EI set-up to determine the thickness of the detector mask septa. Figure 7(b) shows a comparison between the experimental and simulated DM-EI ICs. The detector mask septa thickness was determined to be $28\,\mu m$, which approximately matches the nominal value ($30\,\mu m$), while the sample mask septa are evidently much thinner than this nominal value.

The good agreement between the experimental and simulated ICs shown in Figure 7(a) and (b) demonstrates that the characteristics of the source, sample mask, detector mask and the detector have been modelled satisfactorily. This also means that the model can be used to predict the mixed intensity signal recorded by each system for a known sample in the experimental case.

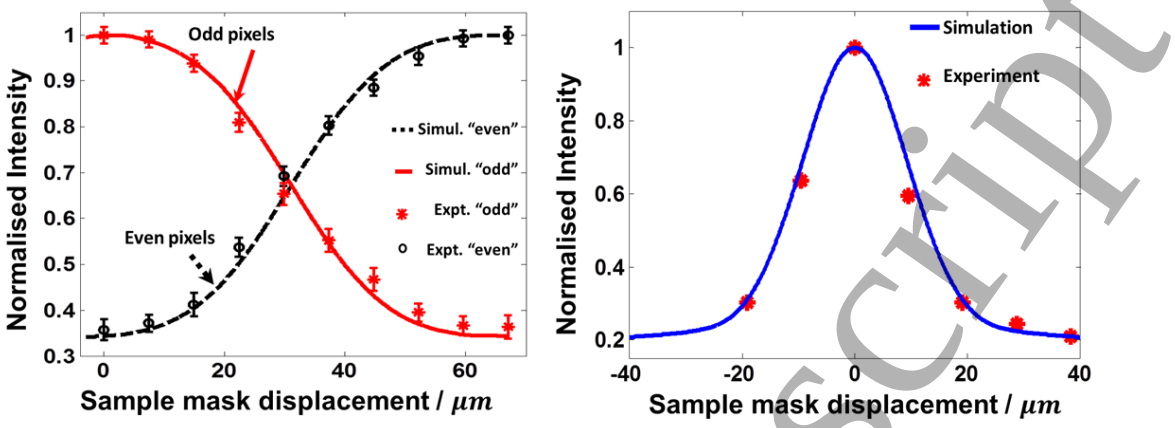

Figure 7(a) The simulated and experimental IC for the single mask EI set-up (a); the two curves are obtained by combining all the "odd" and "even" pixels, respectively. (b) shows the DM-EI ICs also from simulation and experiment.

As previously mentioned, two mixed intensity images are necessary to separate the absorption and differential phase contrast signals. However, for SM-EI, these two images can be acquired simultaneously at the sample mask position where the two "arms" of the IC intersect. At this position both sets of pixels share an equal amount of the incident beam and the two sets of pixels, corresponding to "odd" and "even" columns, are subjected to the previously mentioned "inverted illumination condition", i.e. photons gained by pixel 1 due to refraction are instantaneously lost by pixel 2. This corresponds to the simultaneous detection of positive/negative refraction signals in neighbouring pixels, producing two images with inverted refraction-induced contrasts. Conversely, for the DM-EI set-up, the two images must be acquired with two separate exposures on either side of the IC, with the sample mask displaced in two different positions. This can potentially lead to errors during the acquisition procedure, which would negatively affect the quality of the images.

The capability to acquire two images with inverted refraction contrasts in a single shot makes the SM-EI set-up more dose efficient than its DM-EI counterpart. There are two main ways in which this advantage could be exploited. In the first condition, referred to as SM_1, the statistics collected by the two set-ups is

kept constant, meaning that the total acquisition time and dose delivered to the sample are halved for SM-EI compared to DM-EI, (i.e. $t_{SM_1} = \frac{1}{2} t_{EI}$). In the second approach, referred to as SM_2, the total acquisition time is kept the same in the two cases, ($t_{SM_2} = t_{EI}$). Hence, the dose received by the sample is the same, but higher (double) statistics are collected for the SM-EI set-up. While intermediate conditions are possible, these two modes are useful to study two limiting cases. For example SM_1 could prove particularly useful in applications where the exposure time or dose to the sample should be minimised, while SM_2 might be beneficial when the flux is limited. Since this latter approach more closely corresponds to the current experimental conditions, the SM_2 mode was selected for this comparison. Moreover, the mode was studied to determine whether the increased statistics would sufficiently compensate for the reduction in refraction sensitivity caused by the broadening of the IC, which is predicted by Eqn. (3) for non-ideal detectors.

3. Results

Images of a wire phantom in air were acquired with both set-ups according to image acquisition parameters specified in section 2.1, and details of the wire phantom are provided in the caption of Figure 8. All experimental images were first normalised by a flat field image.

3.1 Evaluating the contrast and SNR in the mixed intensity images

Contrast and SNR were evaluated for each wire in one mixed intensity projection, for the DM and SM-EI systems as follows:

$$\text{Contrast} = \frac{I_{max} - I_{min}}{I_{background}}, \quad \textbf{(5)}$$

$$\text{SNR} = \frac{I_{max} - I_{min}}{2\sqrt{\sigma\left(I_{background}\right)^2}}, \quad \textbf{(6)}$$

where I_{max} and I_{min} are the maximum and minimum signals in each wire profile, respectively, and $\sigma(I_{background})$ is the standard deviation of the image in an adjacent background region. The mixed intensity images are displayed in Figure 8 and were acquired using the second approach (SM_2).

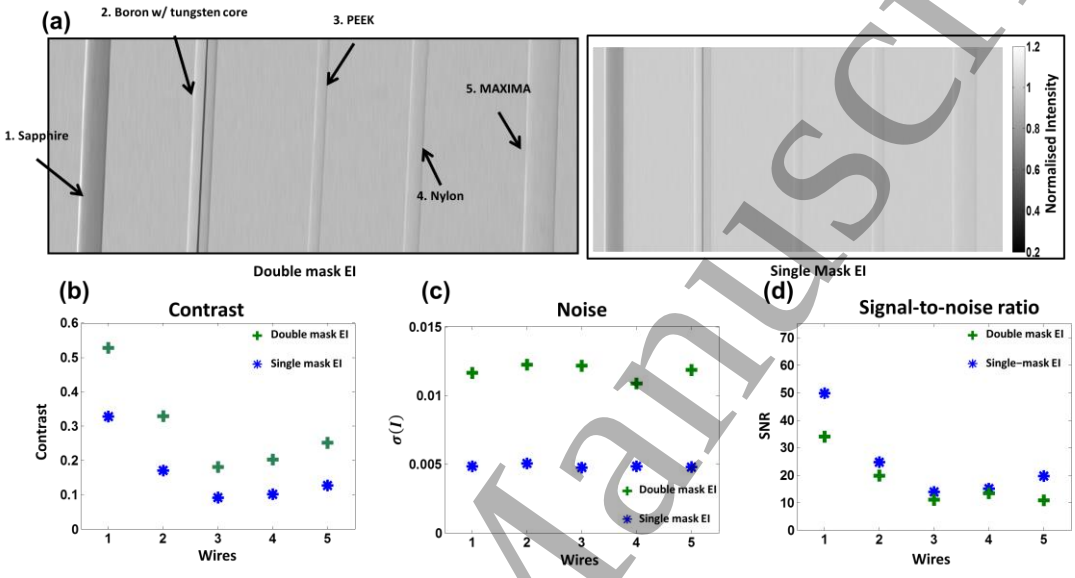

Figure 8 (a) DM-EI and SM-EI experimental mixed intensity projections of a sample consisting of five wires (in air): 1) Sapphire ($radius = 120\,\mu m$), 2) Boron w/ tungsten core ($Boron\ radius = 100\,\mu m$, $Tungsten\ radius = 7\,\mu m$), 3) PEEK ($radius = 60\,\mu m$), 4) Nylon ($radius = 70\,\mu m$) and 5) MAXIMA ($radius = 150\,\mu m$); (b) shows the contrast for each wire in both set ups, (c) shows the noise in the adjacent background regions and (d) shows the signal-to-noise ratio extracted.

Figure 8 shows images of the wire samples acquired with the DM (a) and SM-EI (b) set-ups. These wires were selected because they cover a reasonably wide range of refraction and absorption properties and produce relatively weak USAXS signals. Figure 8(b) shows the peak-to-peak contrast from the five wires, Figure 8(c) shows the average noise in the background regions, and Figure 8(d) is the SNR calculated using the values from the two previous figures. In the DM-EI set-up, each wire possesses a higher contrast than when acquired with the SM-EI set-up. On the other hand, the SNR appears to be higher for the SM-EI set-up, thanks to the aforementioned increase in photon statistics resulting from the use of the

SM_2 approach. In other words, the reduction in noise observed in the single mask case when the same exposure time is used overcompensates for the loss of phase sensitivity, which is made evident by the contrast reduction in the SM-EI case.

3.2 Comparing the experimental results against simulations

From the samples used, the PEEK and sapphire wires were selected for the purposes of comparing simulated and experimental data. These wires were selected as they represent the most extreme examples of weakly/strongly absorbing/refracting objects.

Figure 9(a) and (b) show the experimentally obtained mixed intensity images of the PEEK wire for the DM-EI and SM-EI cases, respectively. Figure 9(c) and (d) show a comparison between the simulated profiles and the experimental ones of the PEEK wire, which are extracted from the red lines shown in the images in Figure 9(a) and (b). Similarly, Figure 9(e)-(h) show the same data for the sapphire wire. There is generally a good agreement between the experimental and simulated profiles. However, for both set-ups, the simulation slightly overestimates the absorption of the sapphire wire through its thickest part. This minor discrepancy can be attributed to imperfect knowledge of the source spectrum and detector energy response function. Furthermore, it is consistent with previous results obtained with a Monte Carlo model of the system, which used the same material data, spectrum, and a linear detector energy response as inputs (Millard et al. 2014). Despite this, it is worth noting that the general shape of the profiles and the reduction in contrast suffered by the wires for the SM-EI set-up are well modelled by the simulation.

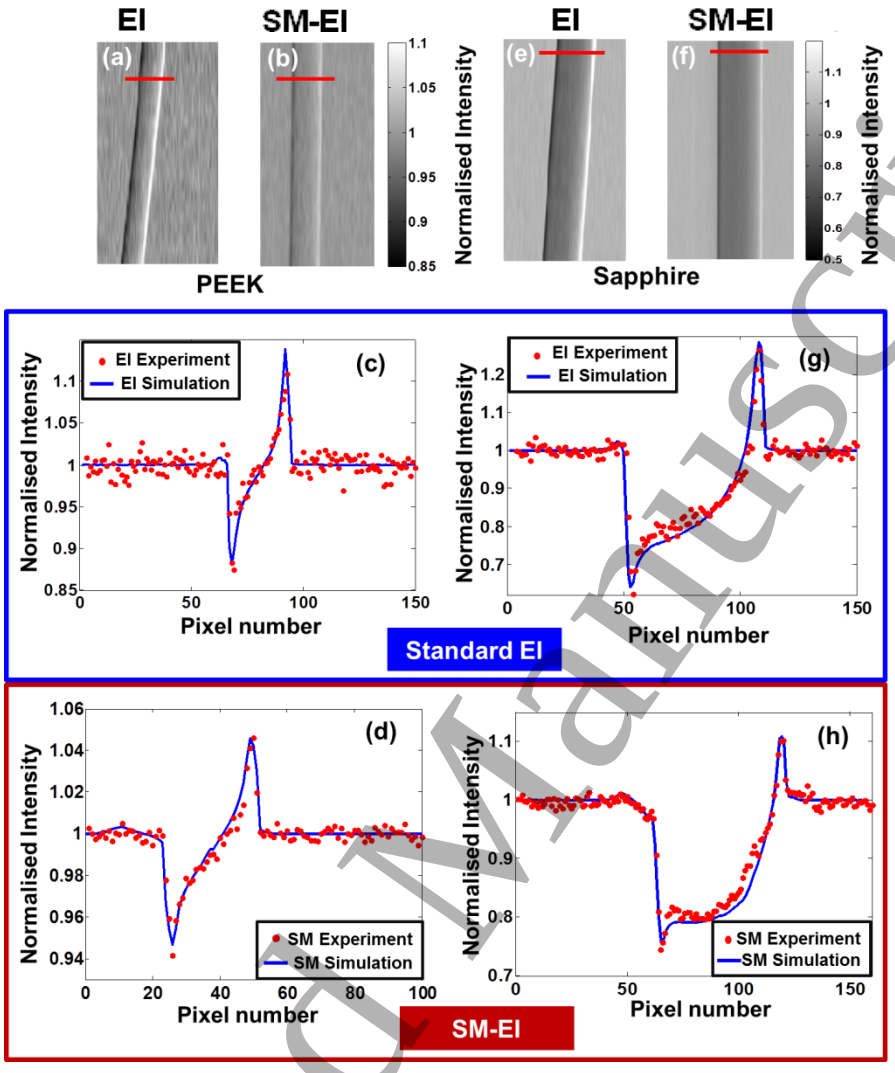

Figure 9 (a) and (b) are mixed intensity images of the PEEK wires acquired with the DM and SM-EI set-ups, and (c) and (d) are their simulated profiles compared against the experimental ones. (e) and (f) show mixed intensity images of the sapphire wire and (g) and (h) show their simulated profiles compared against the experimental ones. All experimental profiles were extracted along the red lines indicated in the images of panels (a), (b), (e) and (f).

Finally, differential phase retrieval was performed on the two sets of images, using the method developed by Diemoz et al (2013). To test the quantitative accuracy of the two EI set-ups, the experimentally retrieved differential phase profiles were compared against their theoretical counterparts, $\tilde{r}$. The latter have been calculated numerically at each energy bin, then weighted by taking into account the approximate x-ray spectrum and detector linear energy response, $spec(E)$, and the transmission through the wire and other optical elements in the set-up $t(E)$ (Munro & Olivo 2013; F.A. Vittoria et al. 2015a), as follows:

$$\tilde{r} = \frac{\sum r(E) \times spec(E) \times t(E)}{\sum spec(E) \times t(E)}. \qquad (7)$$

The differential phase images obtained from experimental data collected with the two set-ups are displayed in Figure 10(a) and (b) for PEEK, and Figure 10(e) and (f) for sapphire, while their profiles are displayed in Figure 10 (c) and (d) (PEEK) and Figure 10(g) and (h) (sapphire).

There is a good agreement between the experimentally measured differential phase profiles and their theoretical counterparts (Figure 10).

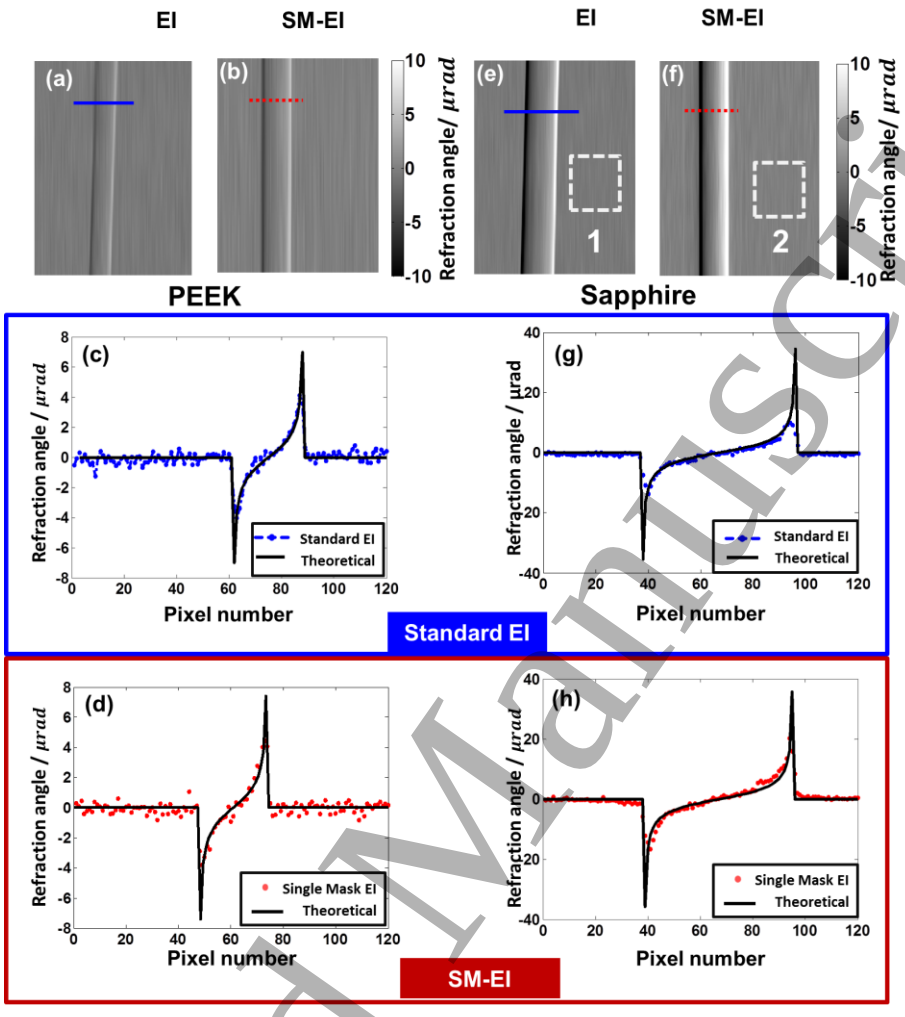

Figure 10 (a) and (b) are differential phase retrieved images of the PEEK wires with DM and SM-EI set-ups and (c) and (d) are the corresponding experimental profiles compared against the theoretical ones. (e) and (f) show differential phase retrieved images of the sapphire wire and (g) and (h) show their experimental profiles compared against the theoretical ones. All experimental profiles were extracted along the blue/red lines indicated in the images of panels (a), (b), (e) and (f); values for the sensitivity for the DM and SM-EI set-ups were measured in background regions 1 & 2 shown in (e) and (f), respectively.

The profiles acquired with the two set-ups are slightly different from one another. The main reason for this is that the theoretical profiles were calculated by taking into account the resultant spectrum for each

set-up. These are different, since for SM-EI the beam only passes through a total of 2 *mm* of carbon (including the detector cover), while there is an added 0.5 *mm* thick layer of carbon in the DM-EI set-up due to the substrate of the additional mask. However, the most likely explanation for the discrepancy between the retrieved profiles relates to the increase in the unwanted transmission through the septa encountered when a thinner mask is used. This means that the sample is simultaneously irradiated by two spectra, one hardened and one not, passing through the mask septa and through the apertures, respectively, as shown in Figure 11(a).

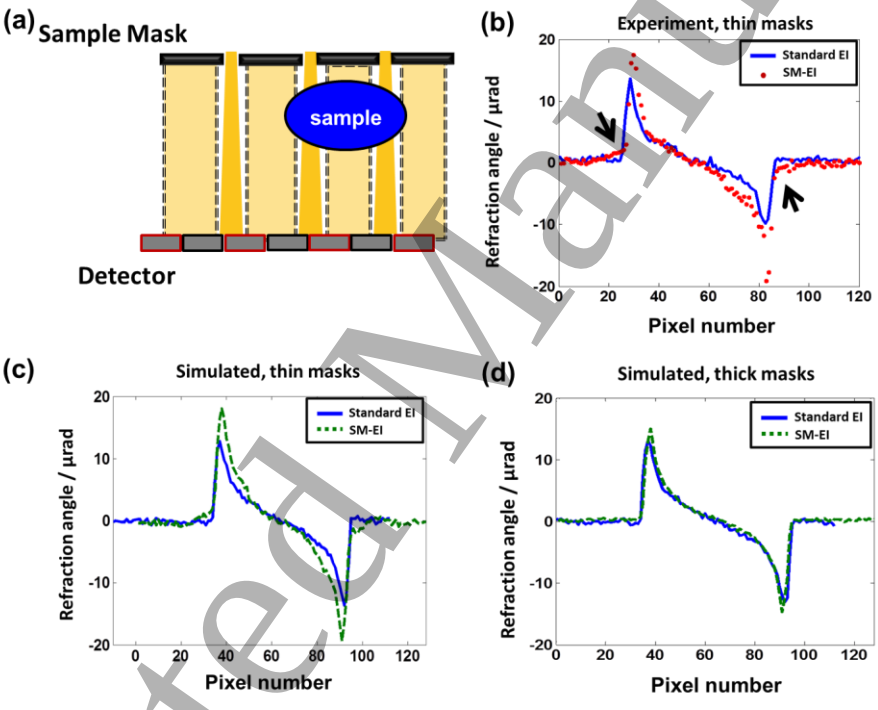

Figure 11 (a) is a schematic depiction of transmission through the mask for SM-EI, (b) shows the phase retrieved profiles of the sapphire wire obtained with DM and SM-EI set-ups compared against each other. In (c) the simulated profiles are compared for the same 17 µm thick mask septa as used in the experiment, while in (d) much thicker mask septa were simulated, equivalent to the total thickness encountered in the DM-EI case (44 µm).

This has an adverse effect on the refraction signal, particularly at the edges of a highly absorbing wire, which is evident in Figure 11(b) for SM-EI, where slight discrepancies can be observed at the edges of the sapphire wire profile. Since similar discrepancies were not observed for PEEK, this confirms that sapphire, being more absorbing, introduces different degrees of additional hardening to parts of the beam going through the septa compared to those parts going only through the apertures. The effect can also be observed in the simulated sapphire wire profiles in Figure 11(c). However, Figure 11(d) demonstrates that the edge discrepancy can be eliminated through the use of thicker masks, in which case the profiles obtained with both DM-EI and SM-EI become identical.

It is important to note that the DM-EI system does not suffer from such effects probably because the combined thickness of the mask septa is sufficient to make effects arising from unwanted transmission negligible. This is somewhat supported by its IC (Figure 7(a)), which has a lower offset (~20%) than the SM-EI IC (~35%).

3.3 Analysing the refraction sensitivity of the DM and SM-EI set-ups

The experimental sensitivity of the two set-ups was then measured by calculating the standard deviation within ROIs in the respective phase retrieved images shown in Figure 10. For the DM-EI set-up, the angular sensitivity was determined to be $280 \pm 10\,nrad$, while for SM-EI it was $350 \pm 10\,nrad$. It should be noted that, as well as reduced steepness of the IC slopes in the SM-EI case, the reduction in the total mask septa thickness also contributes to this sensitivity reduction. The thin pre-sample mask allows increased levels of unwanted transmission through the mask septa, which increases the contributions to the background.

In order to extract an equivalent estimation of the sensitivity from the simulated data, a level of noise comparable to that of the experimental images was added to the simulated mixed intensity profiles, and the sensitivity was extracted from them following the same retrieval procedures outlined above. However, since the noise was added to the simulated profiles after the PSF blurring was applied to the image, the

noise for adjacent detector pixels is totally uncorrelated, which is not necessarily true in the experimental case. Indeed, in the latter case, for large values of σ_{CS}, the noise correlation between adjacent pixels is expected to increase, leading to an apparent increase in sensitivity. However, in the simulated case, the uncorrelated noise is assumed to be a good approximation of the experimental condition since σ_{CS} is small compared to the overall pixel size. The validity of this assumption is further underlined by the good agreement between the sensitivity measured in the simulated and experimental cases for both set-ups. The values extracted for the sensitivity from the background of the simulated DM-EI and SM-EI profiles matched the experimental values: $280 \pm 10\,nrad$ and $350 \pm 10\,nrad$, respectively. While this should be expected given the agreement in the simulated profile and the inclusion of the appropriate level of noise, it further confirms the accuracy of the proposed model. It also means that in these experimental conditions, the DM-EI set-up remains more sensitive than its single-mask counterpart, despite the increase in photon statistics.

3.4 Predicting the refraction sensitivity of EI set-ups for different detector PSFs

The good agreement between experimental and simulated profiles observed in a variety of different conditions indicates that this model can be reliably used to study how the sensitivity varies as a function of the detector PSF.

From Figure 6 and the related discussion, we had concluded that using the detector mask is equivalent to the use of an ideal detector PSF. Therefore, if the total exposure time is kept constant (condition SM_2), it is possible for the sensitivity of the SM-EI set-up to overtake that of the DM-EI set-up at smaller values of σ_{CS}. As σ_{CS} decreases, the sensitivity is expected to increase because the slopes of the PSF, and therefore of the IC, become steeper. Hence, the sensitivity of the SM-EI set-up as a function of σ_{CS} was studied, while keeping the other parameters the same as in the previously described experimental set-up.

Figure 12 shows that, for the SM-EI set-up, there is a gradual increase in the sensitivity as σ_{CS} decreases, as expected. In this configuration, the SM-EI set-up becomes more sensitive to refraction than the DM-EI

set-up when $\sigma_{CS} \leq 5\,\mu m$. Note that when the ideal pixel response is not smoothed by charge sharing effects ($\sigma_{CS} = 0$), the sensitivity of the SM-EI set-up becomes better than the DM-EI set-up by a factor of $\sqrt{2}$, which is thanks to the increase of a factor of 2 in the detected statistics. The sensitivity of the DM-EI set-up, on the other hand, remains constant over the range of simulated σ_{CS} values, which is consistent with the previous observations that the detector mask reproduces the effect of an "ideal" pixel. This analysis was carried out for SM_2 only, for which the exposure time is kept constant across both set-ups; if the same comparison was carried out in the SM_1 configuration, then one would expect the sensitivity of SM-EI to converge to that of DM-EI at $\sigma_{CS} = 0$.

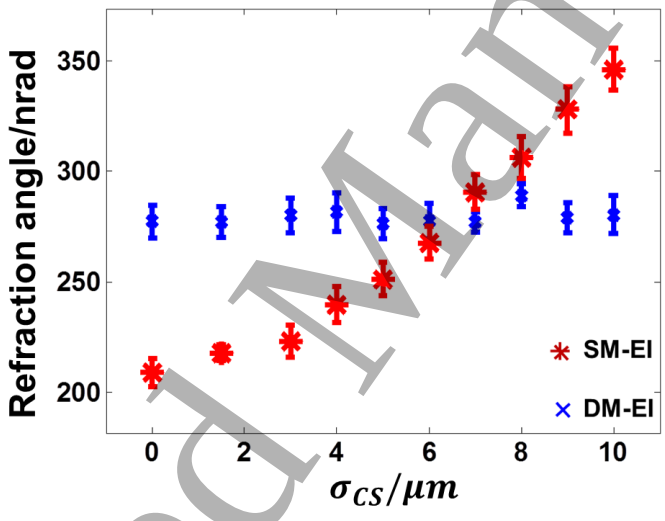

Figure 12 The refraction sensitivity is plotted against different values of σ_{CS}, which are convolved with an ideal pixel function, for both DM-EI and SM-EI set-ups.

4. Discussion and Conclusion

A single-shot EI phase contrast imaging technique was implemented to a commercially available, polychromatic x-ray source with a $FWHM = 70\,\mu m$. The set-up was realised by eliminating the detector mask of the DM-EI system, and using the edges of the detector pixels to directly sense refraction-induced beam displacements. The SM-EI set-up, being very similar to the skipped, DM-EI set-up, could provide

an alternative use of the same system for some applications, especially in biomedical imaging where dithering is not always necessary, and the advantages of the SM-EI set-up can be maximally exploited.

In this study, both set-ups were used to acquire images of wire samples. The mixed-intensity profiles of both strongly and weakly refracting/absorbing samples were selected and compared against those generated with the wave optics simulation for both set-ups. The simulation was designed to accurately model the experimental conditions so that it could also be used to determine parameters of the system, such as mask thickness. As such, the pre-sample mask septa was determined to be thinner than its nominal value, which led to a higher offset in the SM-EI IC, and which was subsequently noted to be responsible for inaccuracies in the phase retrieval algorithm.

The inaccuracies introduced by the high SM-EI IC offset to the measured profiles were attributed to increased x-ray transmission and beam hardening effects, which occur when the beam spectrum passing through the mask septa and apertures undergo additional hardening by a sample with non-negligible absorption. This leads to differences in the retrieved differential phase profiles of the same wire acquired with the two systems. To demonstrate that these were entirely due to insufficient mask thickness, an SM-EI set-up with thick pre-sample mask septa was simulated. In this case, both EI configurations produced identical profiles matching the theoretically calculated ones.

The refraction sensitivity of the two systems was measured experimentally and estimated via simulation, and the values were found to be in agreement. The SM-EI set-up was shown to suffer a slight reduction in its angular sensitivity and contrast. This is well explained by the analytical model for EI refraction sensitivity, proposed by Diemoz et al (2013), which shows that the sensitivity depends on the noise in the image and on the slope of the IC. This notwithstanding, the potential advantages of this modified set-up should not be ignored, especially considering that the sensitivity of the SM-EI set-up can be increased by using a detector with a sharper PSF, such as Pixirad (Delogu et al. 2016). This would make the

advantages of the SM-EI set-up such as simplified alignment, halving the dose, or increased SNR etc. more prominent.

Thus far, the new set-up has only been applied to direct conversion detectors, which typically have pixel sizes $\geq 50\,\mu m$. For smaller (indirect conversion detector) pixels, the beam-tracking set-up can be implemented instead. Although this leads to smaller fields of view and lower detection efficiencies, the use of a high resolution detector in the beam-tracking set-up allows for the single shot extraction of the USAXS signal (in addition to attenuation and refraction), which cannot be done with the proposed set-up.

A simulation model was used to predict the sensitivity of the SM-EI set-up as a function of detector PSF. This showed that the SM-EI set-up becomes more sensitive than the DM-EI one as the detector tends toward ideal behaviour, thanks to the increased number of photons impinging on the detector combined with an increasingly steeper PSF slope.

A system realised using detectors with sufficiently small values of σ_{CS} and employing thicker masks would be more sensitive to refraction than its double mask counterparts, although such a claim warrants further investigation. The clear benefits from such a set-up lie in its simplicity and increased tolerance to misalignments, since only one mask would have to be aligned. However, it imposes the use of a skipped mask, which results either in a resolution decreased by a factor of 2, or requires twice as many dithering steps to achieve the same resolution as the non-skipped, DM-EI set-up. It would also be possible to extend the single mask approach to the 2D-EI system (Kallon et al. 2015), following the method proposed by Krejci et al and defining beamlets that hit the region among four pixels instead of between two (Krejci et al. 2010; Krejci et al. 2011). As well as yielding differential phase signals in 2D in a single-shot, this would also allow for easy, artefact free phase integration with large polychromatic sources.

Acknowledgements

This work was supported by the EPSRC grants (EP/N509577/1, EP/ M507970/1 and EP/1021884/1). ME was supported by the Royal Academy of Engineering under the RAEng Research Fellowships scheme. P.C.D. is supported by the Marie Curie Career Integration Grant PCIG12-GA-2012-333990 within the Seventh Framework Programme of the European Union.

References

F Arfelli, M. Assante, V. Bonvicini, A. Bravin, G. Cantatore, E. Castelli, L. D. Palma, M. Di Michiel, R. Longo, A. Olivo, S. Pani, D. Pontoni, P. Poropat, M. Prest, A. Rashevsky, G. Tromba, A. Vacchi, E. Vallazza and F. Zanconati, Low-dose phase contrast x-ray medical imaging. 1998, *Physics in Medicine & Biology*, 43(10), pp. 2845-52

E. E. Bennett, R. Kopace, A. F. Stein, H. Wen, A grating-based single-shot x-ray phase contrast and diffraction method for in vivo imaging. 2010, *Medical physics* 37(11), pp. 6047-6054.

A. Bravin, P. Coan, & P. Suortti, X-ray phase-contrast imaging: from pre-clinical applications towards clinics. 2013, *Physics in medicine and biology*, 58(1), pp.R1-35.

D. Basta, M. Endrizzi, F. A. Vittoria, G. K. N. Kallon, T. P. Millard, P. C. Diemoz, A. Olivo, Note: Design and realization of a portable edge illumination X-ray phase contrast imaging system. 2015, *Review of Scientific Instruments*, 86(9).

P. Delogu, P. Oliva, R. Bellazzini, A. Brez, P.L. de Ruvo, M. Minuti, M. Pinchera, G. Spandre, A. Vincenzi, Characterization of Pixirad-1 photon counting detector for X-ray imaging. 2016, *Journal of Instrumentation*, 11(1), pp.P01015–P01015.

P. C. Diemoz, C. K. Hagen, M. Endrizzi, A. Olivo, Sensitivity of laboratory based implementations of

edge illumination X-ray phase-contrast imaging. 2013, *Applied Physics Letters*, 103(24), pp.24–29.

P. C. Diemoz, & A. Olivo, On the origin of contrast in edge illumination X-ray phase-contrast imaging. 2014, *Optics express*,22(23), pp.28199–28214.

P. C. Diemoz, F. A. Vittoria, C. K. Hagen, M. Endrizzi, P. Coan, E. Brun, U. H. Wagner, C. Rau, I. K. Robinson, A. Bravin, A. Olivo, Single-image phase retrieval using an edge illumination X-ray phase-contrast imaging setup. 2015, *Journal of Synchrotron Radiation*, 22(4), pp.1072–1077.

M. Endrizzi, P. C. Diemoz, T. P. Millard, J. L. Jones, R. D. Speller, I. K. Robinson, A. Olivo, Hard X-ray dark-field imaging with incoherent sample illumination. 2014, *Applied Physics Letters*, 104(2), pp. 1–4.

M. Endrizzi, F. A. Vittoria, G. Kallon, D. Basta, P. C. Diemoz, A. Vincenzi, P. Delogu, R. Bellazzini, A. Olivo, Achromatic approach to phase-based multi-modal imaging with conventional X-ray sources. 2015a, *Optics Express*, 23(12), p.16473.

M. Endrizzi, D. Basta, & A. Olivo, Laboratory-based X-ray phase-contrast imaging with misaligned optical elements. 2015b, *Applied Physics Letters*, 107(12), pp.10–15.

K. Ignatyev, P. R. T. Munro, D. Chana, R. D. Speller, A. Olivo. Effects of signal diffusion on x-ray phase contrast images. 2011, *Review of Scientific Instruments*, 82(7).

M. Kagias, S. Cartier, Z. Wang, A. Bergamaschi, R. Dinapoli, A. Mozzanica, B. Schmitt, and M. Stampanoni, Single shot x-ray phase contrast imaging using a direct conversion microstrip detector with single photon sensitivity. 2016, *Applied Physics Letters*, 108(23).

G. K. Kallon, M. Wesolowski, F. A. Vittoria, M. Endrizzi, D. Basta, T. P. Millard, P. C. Diemoz, and A. Olivo. A laboratory based edge-illumination x-ray phase-contrast imaging setup with two-directional sensitivity,2015, *Applied Physics Letters*, 107(20).

A. Konstantinidis, Evaluation of digital x-ray detectors for medical imaging applications. 2011 Doctoral thesis, UCL (University College London). Available at: http://discovery.ucl.ac.uk/1322919/.

F. Krejci, J. Jakubek, and M. Kroupa. Hard x-ray phase contrast imaging using single absorption grating and hybrid semiconductor pixel detector. 2010, *Review of Scientific Instruments*, 81(11): 113702.

F. Krejci, J. Jakubek, and M. Kroupa. Single grating method for low dose 1-D and 2-D phase contrast X-ray imaging. 2011, *Journal of Instrumentation*, 6:C01073–C01073.

T. P. Millard, M. Endrizzi, K. Ignatyev, C. K. Hagen, P. R. T. Munro, R. D. Speller, A. Olivo, Method for automatization of the alignment of a laboratory based x-ray phase contrast edge illumination system. 2013, *Review of Scientific Instruments*, 84(8).

T. P. Millard, M. Endrizzi, P. C. Diemoz, C. K. Hagen, A. Olivo, Monte Carlo model of a polychromatic laboratory based edge illumination x-ray phase contrast system. 2014, *Review of Scientific Instruments*, 85(5), p.53702.

A. Momose, Recent Advances in X-ray Phase Imaging. 2005, *Japanese Journal of Applied Physics*, 44(9A), pp. 6355-6367

K. S. Morgan, D. M. Paganin, and K. K.W Siu, Quantitative single-exposure x-ray phase contrast imaging using a single attenuation grid. 2011, *Optics express* 19(20): pp.19781-19789.

K. S. Morgan, P. Modregger, S. C. Irvine, S. Rutishauser, V. A. Guzenko, M. Stampanoni, and C. David, A sensitive x-ray phase contrast technique for rapid imaging using a single phase grid analyser. 2013, *Optics letters* 38(22), pp. 4605-8.

P. R. T. Munro & A. Olivo, X-ray phase-contrast imaging with polychromatic sources and the concept of effective energy. 2013, *Physical Review A - Atomic, Molecular, and Optical Physics*, 87(5).

P. R. T. Munro, K. Ignatyev, R. D. Speller, and A. Olivo, Phase and absorption retrieval using incoherent

X-ray sources. 2012, *Proceedings of the National Academy of Sciences*, 109(35), pp.13922–13927.

P. R. T Munro, Coherent X-ray imaging across length scales. 2017, *Contemporary Physics*, 58(2), pp.1–20. Available at: https://www.tandfonline.com/doi/full/10.1080/00107514.2016.1265771.

A. Olivo, F. Arfelli, G. Cantatore, R. Longo, R. H. Menk, S. Pani, M. Prest, P. Poropat, L. Rigon, G. Tromba, E. Vallazza, and E. Castelli, An innovative digital imaging set-up allowing a low-dose approach to phase contrast applications in the medical field. 2001, *Medical physics*, 28(8), pp.1610–1619.

A. Olivo, F Arfelli , D. Dreossi , R. Longo , R. H. Menk, S. Pani , P. Poropat , L. Rigon , F. Zanconati and E. Castelli, Preliminary study on extremely small angle x-ray scatter imaging with synchrotron radiation. 2002, *Physics in medicine and biology*, 47, pp.469–480.

A. Olivo, & R. Speller, Experimental validation of a simple model capable of predicting the phase contrast imaging capabilities of any x-ray imaging system. 2006, *Physics in medicine and biology*, 51(12), pp.3015–3030.

A. Olivo, K. Ignatyev, P. R. T. Munro, and R. D. Speller, Noninterferometric phase-contrast images obtained with incoherent x-ray sources, 2011. *Applied Optics*, Vol. 50 (12), pp. 1765-1769

A. Olivo, S. Gkoumas, M. Endrizzi, C. K. Hagen, M.B. Szafraniec, P. C. Diemoz, P.R.T. Munro, K. Ignatyev, B. Johnson, J. A. Horrocks, S.J. Vinnicombe, J.L. Jones, R.D. Speller, Low-dose phase contrast mammography with conventional x-ray sources. 2013, *Medical Physics*, 40(9), p.90701.

A. Olivo & E. Castelli, X-ray phase contrast imaging: From synchrotrons to conventional sources. 2014, *Rivista del Nuovo Cimento*, 37(9), pp.467–508.

A. Olivo, I. Robinson, Taking X-ray phase contrast imaging into mainstream applications' and its satellite workshop Real and reciprocal space X-ray imaging. 2014, *Philosophical Transactions of the Royal*

Society A: Mathematical, Physical and Engineering Sciences 372, pp. 20130359.

J. Rizzi, P. Mercere, M. Idir, P. Da Silva, G. Vincent, J. Primot, X-ray phase contrast imaging and noise evaluation using a single phase grating interferometer. 2013, *Optics Express*, 21 (14) pp. 17340-17351

F. A. Vittoria, P.C. Diemoz, M. Endrizzi, L. Rigon, F.C. Lopez, D. Dreossi, P.R.T. Munro, A. Olivo, Strategies for efficient and fast wave optics simulation of coded-aperture and other x-ray phase-contrast imaging methods. 2013, *Applied optics*, 52(28), pp.6940–6947.

F. A. Vittoria, G. K. N. Kallon, D. Basta, P.C. Diemoz, I.K. Robinson, A. Olivo, M. Endrizzi, Beam tracking approach for single-shot retrieval of absorption, refraction, and dark-field signals with laboratory x-ray sources. 2015a, *Applied Physics Letters*, 106(22), p.224102.

F. A. Vittoria, M. Endrizzi, P.C. Diemoz, A. Zamir, U.H. Wagner, C. Rau, I. K. Robinson, A. Olivo, X -ray absorption, phase and dark -field tomography through a beam tracking approach. 2015b, *Scientific Reports*, 5:16318.

H. H. Wen, E.E. Bennett, R. Kopace, A. F. Stein, V. Pai, Single-shot x-ray differential phase-contrast and diffraction imaging using two-dimensional transmission gratings. 2010, *Optics letters* 35 (12): 1932-1934.

S. W. Wilkins, Y. I. Nesterets, T. E. Gureyev, S. C. Mayo, A. Pogany, A. W. Stevenson, On the evolution and relative merits of hard X-ray phase-contrast imaging methods. 2014, *Philosophical Transactions of the Royal Society A: Mathematical, Physical and Engineering Sciences* 372 pp. 20130021

M. C. Zdora, P. Thibault, T. Zhou, F. J. Koch, J. Romell, S. Sala, A. Last, C. Rau, and I. Zanette, X-ray Phase-Contrast Imaging and Metrology through Unified Modulated Pattern Analysis. 2017, *Physical Review Letters* 118 (20), pp. 203903.